Supplemental Materials for
"Gauge-field-induced duality group in metamaterials"

Yan Meng[1,2†], Hong-yu Zou[3†], Naifu Zheng[4†], Linyun Yang[2†], Ruo-Yang Zhang[5], Jingming Chen[2], Xiang Xi[1], Bei Yan[2], Yong Ge[3], Yi-jun Guan[3], Shou-qi Yuan[3], Gui-Geng Liu[6], Zhenxiao Zhu[2*], Hong-xiang Sun[3,7*], Ce Shang[8], Hongsheng Chen[9], Qihang Liu[4*], Yihao Yang[9*], Zhen Gao[2*]

[1]School of Electrical Engineering and Intelligentization, Dongguan University of Technology, Dongguan, 523808, China.

[2]State Key Laboratory of Optical Fiber and Cable Manufacturing Technology, Department of Electronic and Electrical Engineering, Guangdong Key Laboratory of Integrated Optoelectronics Intellisense, Southern University of Science and Technology, Shenzhen 518055, China.

[3]Research Center of Fluid Machinery Engineering and Technology, School of Physics and Electronic Engineering, Jiangsu University, Zhenjiang 212013, China.

[4]State Key laboratory of quantum functional materials, Department of Physics, and Guangdong Basic Research Center of Excellence for Quantum Science, Southern University of Science and Technology, Shenzhen 518055, China.

[5]National Laboratory of Solid State Microstructures, School of Physics, Collaborative Innovation Center of Advanced Microstructures, Nanjing University, Nanjing 210093, China.

[6]Department of Electronic and Information Engineering, School of Engineering, Westlake University, Hangzhou, 310030, China.

[7]State Key Laboratory of Acoustics, Institute of Acoustics, Chinese Academy of Sciences, Beijing 100190, China.

[8]Aerospace Information Research Institute, Chinese Academy of Sciences, Beijing 100094, China.

[9]Interdisciplinary Center for Quantum Information, State Key Laboratory of Modern Optical Instrumentation, College of Information Science and Electronic Engineering, ZJU-Hangzhou Global Science and Technology Innovation Center, Key Laboratory of Advanced Micro/Nano Electronic Devices and Smart Systems of Zhejiang, ZJU-UIUC Institute, Zhejiang University, Hangzhou 310027, China.

[†]These authors contributed equally to this work.

*Corresponding author. Email: zhuzx@sustech.edu.cn (Z.Z.); jsdxshx@ujs.edu.cn (H.X.S.); liuqh@sustech.edu.cn (Q.L.); yangyihao@zju.edu.cn (Y.Y.); gaoz@sustech.edu.cn (Z.G.)

Supplementary Note 1: Duality and self-duality in 1D gauged lattices

We begin by exploring duality in a one-dimensional (1D) periodic system composed of four sites per unit cell, coupled through both positive and negative hopping amplitudes, as schematically illustrated in Figs. S1(a) and S1(b). These sign-alternating couplings are engineered by introducing local $\mathbb{Z}_2 = \{\pm 1\}$ gauge degrees of freedom (DOFs), which form the basis for constructing dual and self-dual configurations. The Bloch Hamiltonian of the 1D system takes the form:

$$H_{1\mathrm{D}} = \omega_0 \mathbb{I}_{4\times 4} + \gamma_{10} t_y + \tau_v \otimes (\vec{v}_x \cdot \vec{\sigma}), \tag{S1}$$

where ω_0 denotes the onsite energy, t_y represents the coupling amplitude along the y-direction, and $\gamma_{\mu\nu} = \sigma_\mu \otimes \sigma_\nu$ is the Kronecker product of two Pauli matrices. The vector $\vec{v}_x = (\mathrm{Re}u_x, \mathrm{Im}u_x)$ is constructed from the real and imaginary parts of the Bloch function $u_x = t(1 + e^{ik_x})$, with t being the coupling amplitude along the x-direction, modulated by the local $\mathbb{Z}_2$ gauge field. The vector $\vec{\sigma} = (\sigma_1, \sigma_2)$ comprises two Pauli matrices acting on the sublattice space.

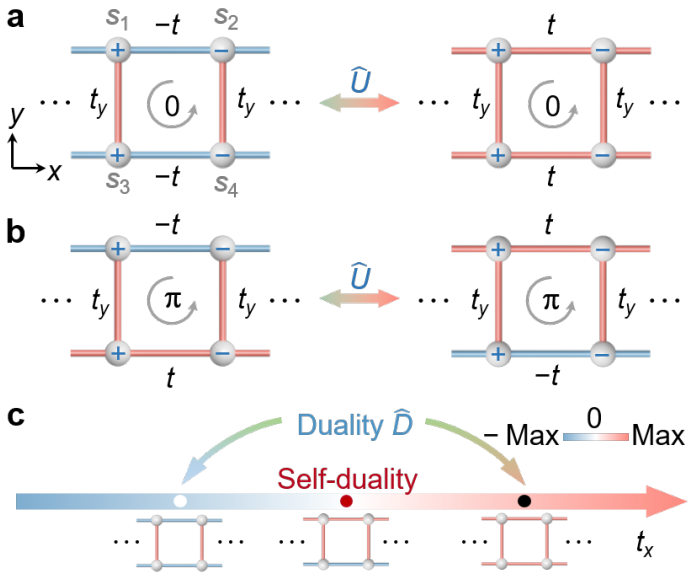

Fig. S1. Gauge-field-induced duality and self-duality in 1D lattices. Red and blue bonds represent positive and negative couplings, respectively. (a) Two distinct lattices are related by a gauge transformation $\hat{U}$, indicated by the "+" and "−" signs on each site (s_1, s_2, s_3, s_4). (b) A self-dual lattice with one positive and one negative coupling along the x-direction, remaining invariant under the same gauge transformation $\hat{U}$. (c) Schematic of the duality mapping $\hat{D} = \hat{U}\hat{\theta}$ in the parameter space of t_x, illustrating that lattices with t_x and $-t_x$ are dual partners, and the $t_x = 0$ point corresponds to a self-

dual configuration.

In the 1D system, the parameter ν encodes the symmetry class: $\nu = 0$ corresponds to the dual lattices [Fig. S1(a)], while $\nu = 3$ characterizes the self-dual lattice [Fig. S1(b)]. These configurations are distinguished by their distinct gauge flux patterns. The effective gauge flux Φ enclosed by each plaquette is defined as [1–8]:

$$\exp(i\Phi) = \prod_{\langle m,n \rangle} \mathrm{sign}\left(t_{m,n}\right), \tag{S2}$$

where $t_{m,n}$ denotes the coupling between sites s_m and s_n. The flux Φ takes quantized values of 0 or π, as labeled in Fig. S1. These gauge fluxes characterize the topological nature of the system and are essential to realizing duality and self-duality driven by artificial gauge fields.

Transformations between different configurations in Fig. S1(a) can be realized via a local gauge transformation $\hat{U}$, specified by assigning a $\{\pm 1\}$ sign to each site. This unitary operator reverses the couplings between s_m and s_n with opposite signs. For simplicity, we denote the sum of couplings along the *x*-direction (with equal absolute value) as t_x. Under the gauge transformation operator $\hat{U}$, the 1D Hamiltonian transforms as:

$$\hat{U}\hat{H}_{1D}(t_x, t_y, k_x)\hat{U}^{-1} = \hat{H}_{1D}(-t_x, t_y, -k_x). \tag{S3}$$

where $\hat{U} = \gamma_{03}\hat{\mathbb{I}}_4$ is a unitary matrix ($U \circ U^{+} = \mathbb{I}_4$). By combining $\hat{U}$ with an anti-unitary time-reversal operator $\hat{\Theta}$, we define the duality operator $\hat{D} = \hat{U}\hat{\Theta}$ ($D^2 = -\mathbb{I}_4$). Owing to the time-reversal symmetry, $\hat{\Theta}\hat{H}(t_x, t_y, -k_x)\hat{\Theta}^{-1} = \hat{H}(t_x, t_y, k_x)$, the duality correlation can be expressed:

$$\hat{D}\hat{H}(t_x, t_y, k_x)\hat{D}^{-1} = \hat{H}(-t_x, t_y, k_x). \tag{S4}$$

This correlation ensures that any two Hamiltonians related by $\hat{D}$ share identical eigenvalues, which can be proved as follows.

Suppose $\hat{H}_2 = \hat{D}\hat{H}_1\hat{D}^{-1}$, then their eigenvalue equations can be given:

$$\hat{H}_1|\psi\rangle = \omega_1|\psi\rangle, \quad \hat{H}_2|\phi\rangle = \omega_2|\phi\rangle. \tag{S5}$$

Substituting $\hat{D}\hat{H}_1\hat{D}^{-1}$ into Eq. (S5) we have:

$$\hat{H}_2|\phi\rangle = \hat{D}\hat{H}_1\hat{D}^{-1}|\phi\rangle = \omega_2|\phi\rangle. \tag{S6}$$

The anti-unitary operator contains a complex operator $\hat{\Theta}$, which will reverse the

eigenvalues from ω to ω^*. Since $\omega \in \mathbb{R}$ for Hermitian systems, $\omega^* = \omega$. Applying the duality operator $\hat{D}$ to both sides of the first equation in Eq. (S5), we obtain:

$$\hat{D}\hat{H}_1|\psi\rangle = \hat{D}(\omega_1|\psi\rangle) = \omega_1^* \hat{D}|\psi\rangle = \omega_1 \hat{D}|\psi\rangle \quad \text{(S7)}$$

Substituting $\hat{D}\hat{H}_1 = \hat{H}_2\hat{D}$ into Eq. (S7) yields:

$$\hat{D}\hat{H}_1|\psi\rangle = \hat{H}_2\big(\hat{D}|\psi\rangle\big) = \omega_1\hat{D}|\psi\rangle \quad \text{(S8)}$$

Thus, $\hat{D}|\psi\rangle$ is an eigenvector of $\hat{H}_2$ with the same eigenvalue ω_1, demonstrating that two dual systems possess identical band structures. In the self-dual case [Fig. S1(b)], the lattice maps onto itself under a gauge transformation $\hat{U}$. The self-dual Hamiltonian $\hat{H}_s$ is invariant under a duality operator $\hat{D}$ (i.e., $\hat{D}\hat{H}_s\hat{D}^{-1} = \hat{H}_s$), necessarily features doubly degenerate eigenvalues.

To rigorously verify this, we apply $\hat{D}$ on the eigenvalue equation $\hat{H}_s|\psi\rangle = \omega|\psi\rangle$, and obtain:

$$\hat{H}_s\hat{D}|\psi\rangle = \hat{D}\hat{H}_s|\psi\rangle = \omega\hat{D}|\psi\rangle, \quad \text{(S9)}$$

i.e., $\hat{D}|\psi\rangle$ is another eigenstate of H_s with the same eigenvalue ω. To prove $\hat{D}|\psi\rangle$ and $|\psi\rangle$ are orthogonal, we first assume $\hat{D}|\psi\rangle$ and $|\psi\rangle$ are parallel, i.e., $\hat{D}|\psi\rangle = e^{i\phi}|\psi\rangle$. Applying an extra $\hat{D}$ operator on both sides of Eq. (S9):

$$\hat{D}^2\big|\psi\rangle = \hat{D}e^{i\phi}\big|\psi\rangle = e^{-i\phi}\hat{D}|\psi\rangle = |\psi\rangle, \quad \text{(S10)}$$

which contradicts the condition $\hat{D}^2 = -1$. Hence, $\hat{D}|\psi\rangle$ and $|\psi\rangle$ are orthogonal, forming a Kramers-like doublet feature for the self-duality lattice despite the absence of intrinsic spin.

As illustrated in Fig. S1(c), lattices with coupling amplitudes t_x and $-t_x$ are dual partners and thus acquire identical band structures. When $t_x = 0$, the lattice becomes self-dual, and all bands are doubly degenerate, enforced by duality.

Supplementary Note 2: Realization of positive and negative couplings in acoustic metamaterials

Negative coupling is essential for constructing $\mathbb{Z}_2$ gauge fields and generating non-zero gauge fluxes. In acoustic metamaterials, such negative coupling can be realized through a coupled dipole mechanism. As shown in Fig. S2(a), when two p_y-like dipole modes

couple, their eigenfrequencies split into two distinct eigenfrequencies, one corresponding to an in-phase coupled mode and the other to an out-of-phase mode. The coupling strength is denoted by κ. For negative coupling ($\kappa < 0$), the in-phase mode has a lower energy than the out-of-phase mode. Conversely, for positive coupling ($\kappa > 0$), the in-phase mode exhibits a higher energy.

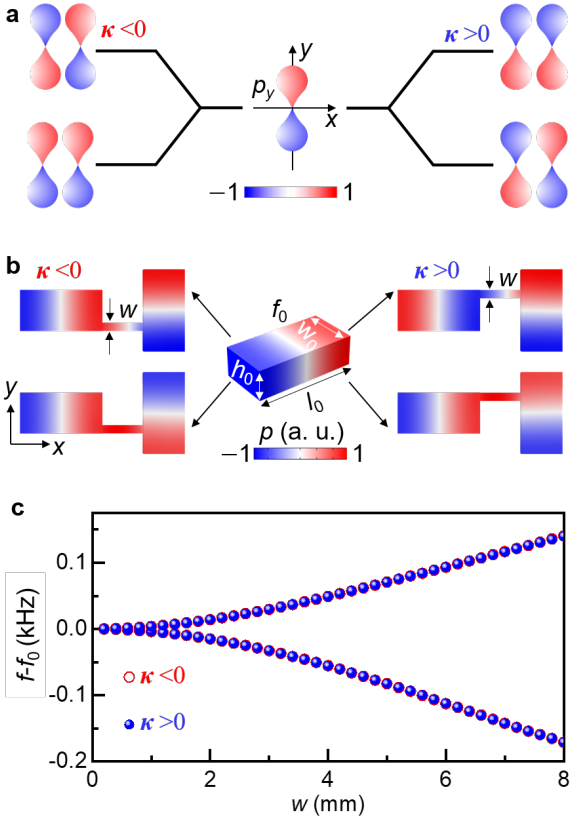

Fig. S2. (a) Schematic of coupled dipole modes. For positive coupling $\kappa > 0$ the in-phase mode exhibits a higher frequency than the out-of-phase mode. For negative coupling $\kappa < 0$, the in-phase mode exhibits a lower frequency than the out-of-phase mode. (b) A single acoustic resonator with dimensions $l_0 = 40$ mm, $w_0 = 20$ mm, and $h_0 = 12$ mm supports a dipole-like mode at $f_0 = 4310$ Hz. Positive and negative couplings are realized by connecting two acoustic resonators at different positions with a coupling tube of width w. (c) Coupling strengths (mode splitting) for positive (blue spheres) and negative (red open circles) couplings versus the coupling tube width w.

The physical implementation of this mechanism is illustrated in Fig. S2(b). All numerical results presented in this work are obtained using the commercial finite element method software COMSOL Multiphysics (Pressure Acoustics, Frequency Domain). All eigenfrequency spectra are solved with the Eigenfrequency solver. The

background surrounding and filler of the acoustic system are air at 25 ℃ (an acoustic velocity of $c_0 = 345\ \mathrm{m/s}$ and an air density of $\rho_0 = 1.19\ \mathrm{kg/m^3}$). A cuboid acoustic resonator with sound-hard boundary conditions on all outer surfaces supports a dipole-like resonance mode at an eigenfrequency of $f_0 = 4310$ Hz. The coupling between two resonators gives rise to two coupled dipole modes exhibiting eigenfrequency splitting. The coupling strength κ is extracted from the magnitude of this splitting and is tunable by adjusting the width w of the coupling tube. Specifically, the sign of the coupling is controlled by the relative position of the coupling connection: when the in-phase mode possesses a higher eigenfrequency than the out-of-phase mode, the coupling is positive ($\kappa > 0$); conversely, if the in-phase mode has a lower eigenfrequency, the coupling is negative ($\kappa < 0$). This positional control enables flexible realization of both positive and negative couplings within the same design framework.

The coupling strength, characterized by the mode splitting as a function of the coupling width w, is shown in Fig. S2(c). Blue spheres indicate positive coupling ($\kappa > 0$), while red open circles represent negative coupling ($\kappa < 0$). As w increases, the magnitude of the coupling (i.e., the frequency splitting) increases as well, demonstrating the tunability of the coupling strength. This flexible control over both the sign and strength of the coupling enables the implementation of artificial gauge fields, facilitating the exploration of $\mathbb{Z}_2$-gauge-field-induced duality and self-duality in acoustic metamaterials.

Supplementary Note 3: Experimental demonstration of the duality and self-duality in 1D acoustic metamaterials

To experimentally demonstrate the features of duality and self-duality, namely the identical band structure for dual lattices and the Kramers-like double degeneracy in a self-dual lattice, a pair of dual acoustic metamaterials and a self-dual acoustic metamaterial are designed and fabricated using standard three-dimensional (3D) printing technology. An example of a duality metamaterial is shown in Fig. S3 (a). The metamaterial boundaries, with a thickness of 3 mm, act as hard walls enclosing air-

filled hollow regions. The unit cell, indicated by a red dashed rectangle with a lattice constant $a = 100$ mm, consists of four cuboid acoustic cavities, four intracell, and four intercell coupling tubes. The geometric details of each unit cell are shown in Fig. S3 (b). Each cavity has the same dimensions as used in the simulations: a length of 40 mm, a width of 20 mm, and a height of 12 mm. The side lengths of the intracell and intercell coupling tubes are 3 mm and 6 mm, respectively. The positions of the coupling tubes along the *x*-direction are described by a distance $d + \Delta d$, where $d = 50$ mm is a reference center-to-center distance, and Δd introduces asymmetry. The coupling amplitude between cavities is determined by both the cross-section and the connection position of the coupling tubes. By fixing the tube cross-section while tuning Δd, the coupling along the *x*-direction can be continuously adjusted. Specifically, the negative (positive) coupling is realized for $\Delta d < 0$ ($\Delta d > 0$), and $\Delta d = 0$ leads to a configuration with equal-magnitude positive and negative couplings.

The measured band structures, obtained from the spatial fast Fourier transform of the complex acoustic pressure fields, are plotted as color maps in the left and right panels of Fig. S3(c), which correspond to two dual metamaterials with $\Delta d = -17$ mm and Δd =17 mm, respectively. Despite their distinct structural configurations, the two acoustic metamaterials exhibit identical band structures, thereby verifying the duality mappings. The center panel presents the measured results for the self-dual metamaterial (Δd =0), revealing twofold degenerate bands across the entire first Brillouin zone (FBZ). This degeneracy originates from the invariance of the self-dual metamaterial under the duality operator $\widehat{D}$.

For comparison, the band structures calculated from the analytical model in Eq. (S1) are plotted as solid and dashed lines in Fig. S3(c). The parameters used are a resonant frequency $\omega_0 = 4310$ Hz and dimerized couplings along the *x*-direction, expressed as $u_x = t_1 + t_2 e^{ik_x}$, with $t_y = t_1 = 31$ Hz, and $t_2 = 103$ Hz. The excellent agreement between the measured and analytical results convincingly validates the accuracy of our theoretical model and supports the feasibility of realizing dual and self-dual acoustic metamaterials with artificial gauge fluxes. The duality mappings between acoustic

metamaterials and self-duality metamaterials are schematically illustrated in Fig. S3(d). It can be seen that metamaterials with opposite Δd values are mapped onto each other by a duality operator, whereas the self-dual metamaterial with $\Delta d = 0$ maps onto itself, resulting in the characteristic twofold degeneracy across the band structure. These results systematically demonstrate the validity of our strategy for constructing acoustic metamaterials that exhibit duality and self-duality enabled by artificial gauge fields.

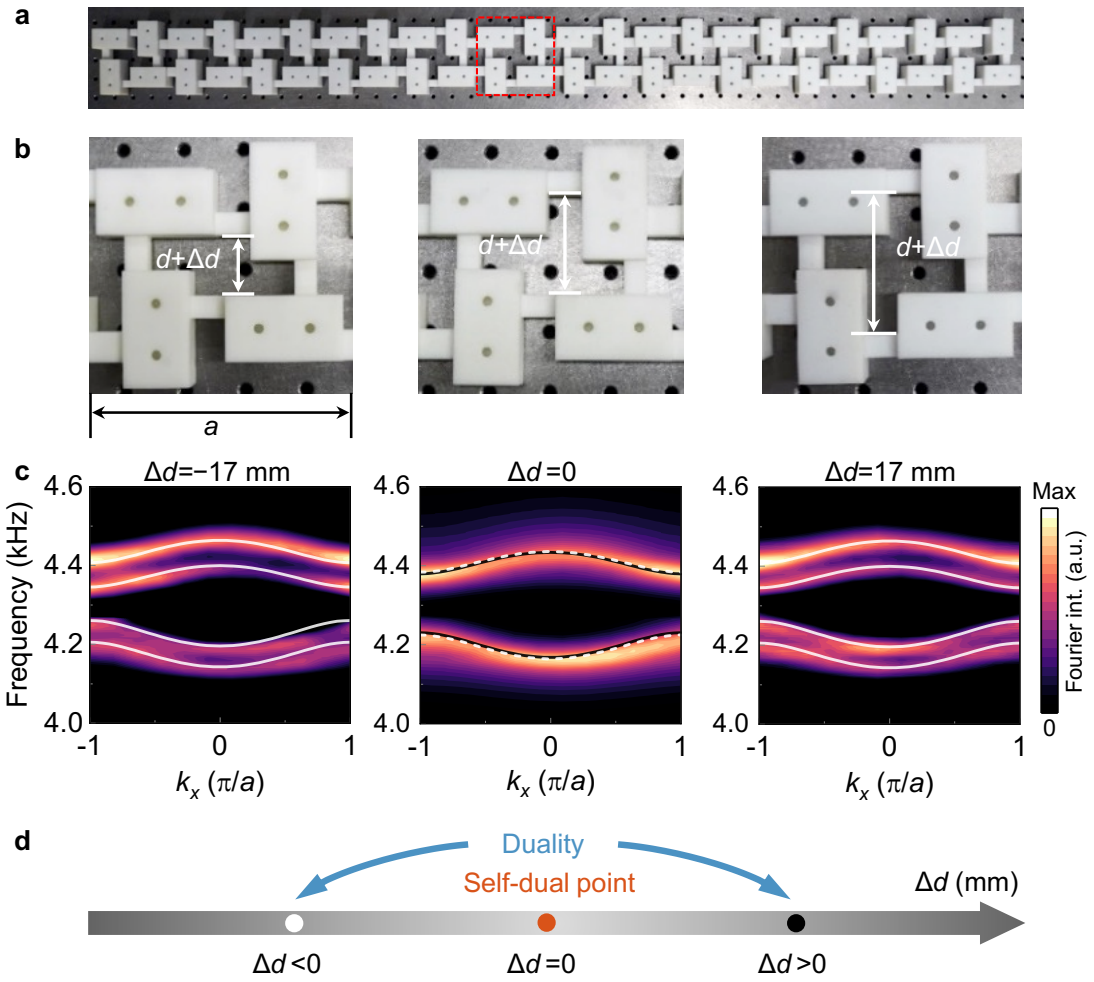

Fig. S3. Experimental demonstration of duality and self-duality in 1D acoustic metamaterials. (a) Photograph of a dual metamaterial consisting of 12 unit cells along the x-direction. (b) Unit cells (with lattice constant a) for two dual acoustic metamaterials (left and right panels) and a self-dual acoustic metamaterial (center panel). The coupling configurations along the x-direction are determined by the geometric parameter $d + \Delta d$ (with $d = 50$ mm), corresponding to $\Delta d < 0$, $\Delta d = 0$, and $\Delta d > 0$ for the left, center, and right panels, respectively. (c) Measured band structures (background colors) and corresponding analytical results (solid and dashed

lines) for metamaterials with $\Delta d = -17$ mm (left), $\Delta d = 17$ mm (right), and $\Delta d = 0$ (center). (d) Schematic illustration of the duality transformation, acoustic metamaterials with opposite Δd values are dual to each other under a dual operator $\widehat{D}$, while the self-dual metamaterial with $\Delta d = 0$ remains invariant under $\widehat{D}$.

Supplementary Note 4: Higher-order topological phases in 2D self-dual acoustic metamaterials

In this section, we will discuss the higher-order topological phases in a 2D self-dual lattice. The tight-binding model for a 2D lattice can be given in a matrix form:

$$H_{2\mathrm{D}} = \begin{pmatrix} \omega_0 & t_{x1}u_x^* & t_{y1}u_y & 0 \\ t_{x1}u_x & \omega_0 & 0 & t_{y1}u_y \\ t_{y1}u_y^* & 0 & \omega_0 & -t_{x1}u_x^* \\ 0 & t_{y1}u_y^* & -t_{x1}u_x & \omega_0 \end{pmatrix}, \tag{S11}$$

where ω_0 indicates the onsite energy, $u_{x,y} = (1 + c_{x,y}\, e^{ik_{x,y}})$ is the Bloch function, c_x and c_y are the dimerized ratios between the intercell and the intracell coupling amplitudes along *x* and *y* directions, respectively. The lattice configurations shown in the top panel of Fig. S4 possess three positive and one negative bond, implying that all these self-dual lattices carry a π-gauge flux, and the dimerized couplings are indicated by coupling bonds with larger radii. For the self-dual lattice, the doubly degenerate band spectrum is protected by the self-dual operator $\widehat{D}$ (see demonstration in Supplementary Note 1). As shown in Fig. S4(a), when all coupling amplitudes are equal ($t_x = t_y$), a fourfold degenerate Dirac point can be observed at the *M* point in Fig. S4(b). The eigenfrequency spectrum of a finite-size lattice with open boundary along the *x*-direction is shown in Fig. S4(c), in which the projective bulk band structure (blue lines) as a function of k_y is gapless .

Upon introducing dimerization along the *x*-direction ($t_{x2} > t_{x1}$), as depicted in Fig. S4(d), a bulk bandgap opens at the *M* point in the twofold-degenerate band structure [Fig. S4(e)]. Within this bandgap, Möbius-twisted boundary states [1,4,5] emerge [Fig. S4(f)], indicated by red lines, while bulk bands are shown in blue. The colored dots encode phase information extracted from the phase difference between two neighboring

sublattices (e.g., s_1 and s_3) within each unit cell [4].

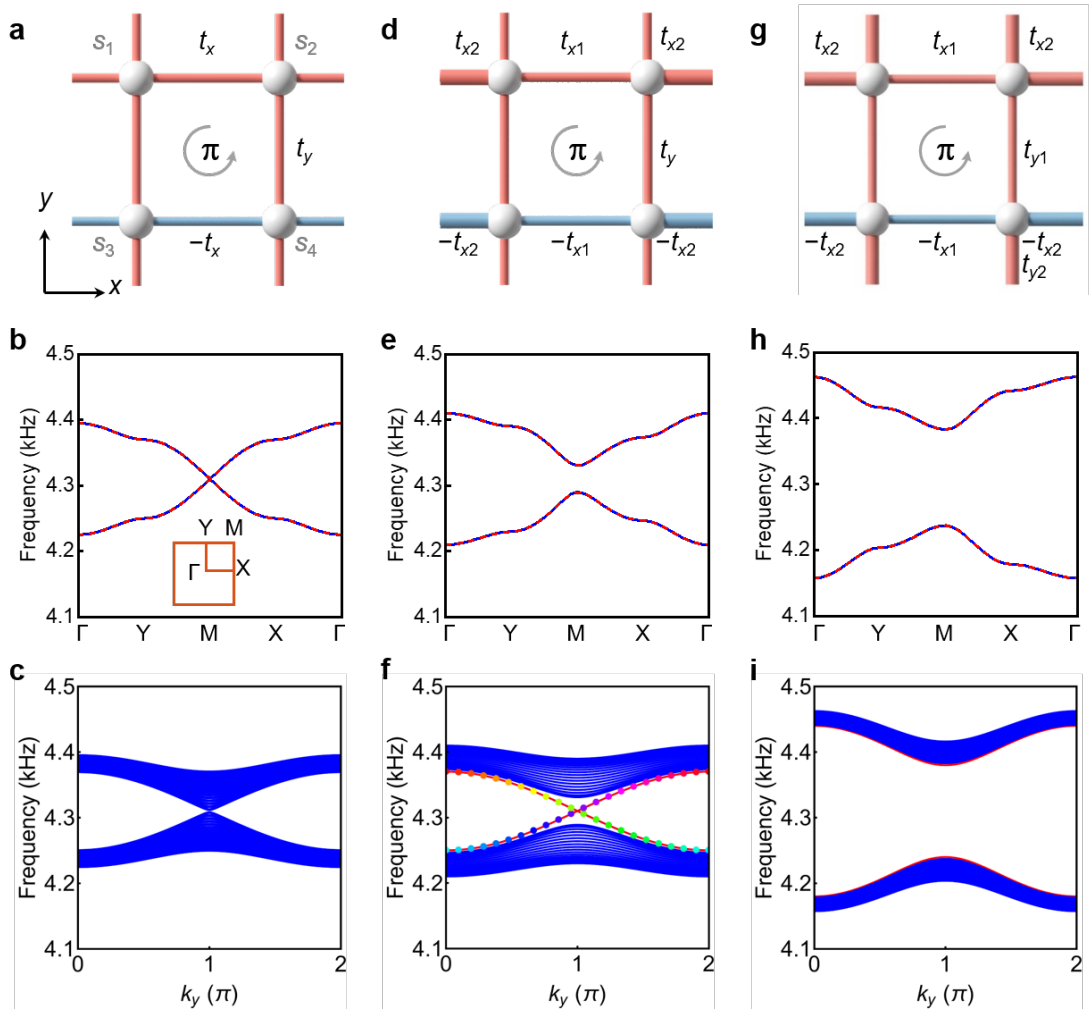

Fig. S4. Configurations and topological band structures of 2D self-dual lattices. Top panel: (a) "Isotropic" lattice with $t_x = t_y$; (d) dimerized coupling along x-direction with $t_{x2} > t_{x1} = t_y$; (g) dimerized coupling along both x and y with $t_{x2}, t_{y2} > t_{x1}, t_{y1}$. Middle panel: Band structures featuring (b) a fourfold degenerate Dirac point at the M point, (e) the Möbius-twisted topological phase, and (h) the higher-order topological phase. Bottom panel: Eigenfrequency spectra for lattices with an open boundary along x. (c) gapless bulk band, (f) Möbius-twisted topological edge states within a non-trivial bandgap, and (i) a higher-order topological bandgap with gapped edge states.

With further dimerization along the y-direction, such that $t_{y2} > t_{y1}$, as depicted in Fig. S4(g), the bulk bandgap is enlarged, as shown in Fig. S4(h). Consequently, a topological bandgap opens, gapping out the previously gapless Möbius-twisted edge states, as illustrated in Fig. S4(i). This additional dimerization along both spatial directions enables the realization of a higher-order topological insulator—specifically,

a quadrupole topological insulator—within the self-dual system [9].

To experimentally demonstrate the higher-order topological insulator in the self-dual system, we fabricate a metamaterial consisting of 12×12 unit cells. As shown in Fig. S5(a), the detailed configuration of a single unit cell is provided in the upper-right inset, while the corresponding tight-binding model featuring dimerized couplings and a π-gauge flux is illustrated in the lower-left inset. Compared to the structure in Fig. 2(b) of the main text, the side lengths of the intercell coupling tubes are increased from 3 mm to 4 mm along the x-direction and 6 mm along the y-direction. The measured band structure for the metamaterial is presented as a color map in Fig. S5(b), revealing a doubly degenerate band structure with a clear bandgap. For validation, simulated results are plotted as black and white lines, exhibiting excellent agreement with the experimental results. All band structures, in this work, are solved with the Eigenfrequency solver. Floquet periodic boundary conditions are imposed on periodic surfaces of the unit cell along both the x and y directions for the 2D system, while sound hard boundary conditions are applied on all the other outer surfaces. The eigenfrequency spectrum of the finite-size system (12×12 unit cells) is shown in Fig. S5(c), where topological edge states (blue circles) and fourfold-degenerate corner states (red dots) are unambiguously observed within the bulk band (gray dots). A zoomed-in view of the fourfold-degenerate corner states is highlighted in the black dashed rectangle.

In Fig. S5(d), we plot the measured average acoustic intensity for the regions highlighted in red, blue, and gray in the inset. Each acoustic resonator includes two holes, and the acoustic intensity is measured by exciting one hole and detecting the response from the other. The total intensity within each region is averaged over the number of resonators. As predicted, a dip between two gray peaks indicates the bulk bandgap, while a dip between two blue peaks corresponds to the gapped 1D edge states. A prominent peak located within the common gap between the bulk and edge states explicitly verifies the existence of zero-dimensional (0D) topological corner states.

The measured spatial distributions of pressure amplitude $|p|$ for the topological edge

states (near 4350 Hz) and corner states (near 4310 Hz) are shown in Fig. S5(e)-(f), respectively. The field pattern of the edge state shows strong localization along the upper boundary of the metamaterial, while the corner states are sharply confined at the

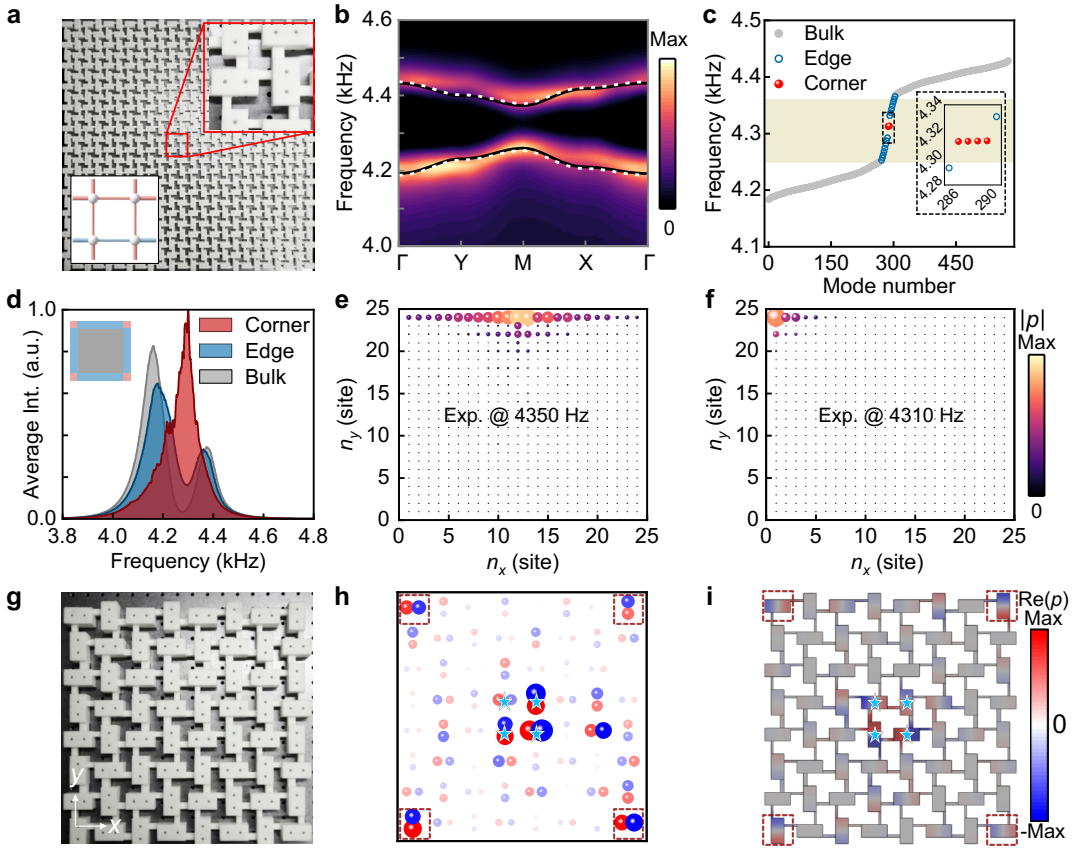

Fig. S5. Higher-order topological phases in the self-dual acoustic metamaterial. (a) Photograph of the fabricated metamaterial consisting of 12×12 unit cells. Upper-right inset: zoom-in view of a single unit cell. Lower-left inset: tight-binding model with π-gauge flux, where the dimerized couplings are indicated by coupling tubes of different radii. (b) Measured (color map) and numerically calculated (solid and dashed lines) band structures, showing a clear bandgap. (c) Eigenfrequency spectrum of the metamaterial, featuring topological edge (blue) and corner (red) states within the bulk bands (gray). Inset: enlarged view of the fourfold-degenerate corner states. (d) Measured average intensity spectra for bulk (gray), edge (blue), and corner (red) regions (indicated in the inset). (e), (f) Measured pressure amplitude distributions $|p|$ for topological edge (e) and corner (f) states. (g) Photograph of a smaller metamaterial containing 4×4 unit cells for simultaneous excitation of all corner states. (h), (i) Measured (h) and simulated (i) pressure field distributions Re(p), showing dipole-like localization of corner states. Blue stars indicate excitation positions, and red dashed rectangles mark the region of corner localization.

corners, in agreement with the expected characteristics of higher-order topological modes. Since the corner states are degenerate and spatially localized at each corner of the metamaterial, it is possible to simultaneously excite all four corner states. To decrease the influence of viscous losses in the air-filled regions of the metamaterial, a smaller sample comprising 4×4 unit cells is fabricated, as depicted in Fig. S5(g). Four point sources (indicated by blue stars) are placed at the central sites of the metamaterial to simultaneously and symmetrically excite the corner states. The corresponding measured and simulated field distributions of the real part of the acoustic pressure [Re(p)] are shown in Figs. S5(h) and S5(i), respectively. In both cases, clear dipolar field profiles are observed, with strong localization at the four corners, confirming the simultaneous excitation of all four corner states. These results provide unambiguous experimental verification of higher-order topological phases in a self-dual acoustic metamaterial platform through comprehensive measurements.

Supplementary Note 5: Self-duality for 3D lattices with 6π gauge flux

For lattices belonging to the duality group carrying 2π and 4π gauge flux, mutual transformations can be achieved via gauge transformations, as shown in Figs. S6(a) and S6(b). Taking two representative lattices from each group as examples, Figs. S6(d) and S6(e) demonstrate that they can be mapped onto each other via the gauge transformation operator $\widehat{U}_5 = \mathrm{diag}(1,1,1,1,-1,1,-1,1)$. In contrast, lattices within the self-duality group carrying 6π gauge flux remain invariant under the action of $\widehat{U}_5$, modulo a spatial symmetry transformation (G_p) or a global sign flipping ($\mathcal{G}$). The gauge transformations illustrated in Fig. S6, together with those shown in Fig. 3 of the main text, substantiate the theoretical prediction that self-dual lattices with 6π gauge flux are invariant under all duality operations associated with the duality group carrying 0-gauge flux and the self-duality groups carrying 2π and 4π gauge flux.

In the 6π-gauge flux configuration, the Hamiltonian is invariant under the combination of gauge transformation ($\widehat{U}_5$), and time reversal symmetry $\hat{\theta}$, forming the duality symmetry $\widehat{D}_5 = \widehat{U}_5\hat{\theta}$ with $(D_5)^2 = -1$. This duality enforces a Kramers-like

twofold degeneracy across the entire Brillouin zone. Additionally, the SU(2) spin-rotation symmetry guarantees that every band is at least doubly degenerate. Since the SU(2) symmetry generators commute with the duality operator, one can construct four mutually orthogonal degenerate eigenstates, implying that the energy bands are at least fourfold degenerate throughout the entire BZ.

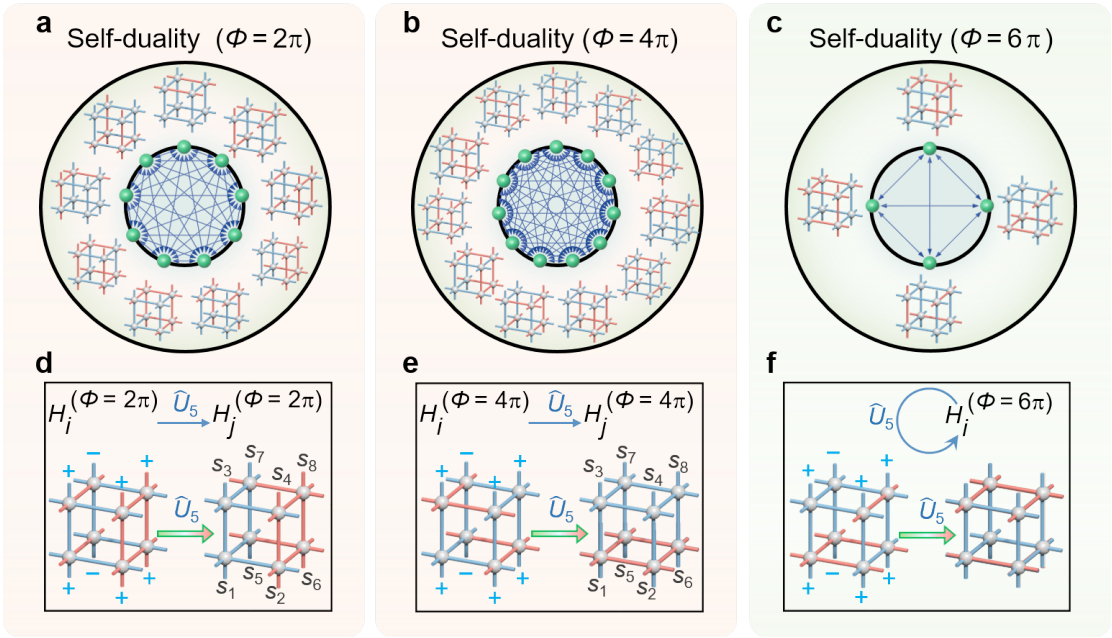

Fig. S6. Self-duality in 3D lattices with 6π gauge flux. (a)-(c): Representative lattice configurations from the duality group with 2π, 4π, and 6π gauge flux. (d)-(e) Gauge transformations between dual lattice configurations shown in (a) and (b), mediated by the operator $\widehat{U}_5$. (f) Invariance of the self-dual lattice with 6π gauge flux under the same gauge transformation operator.

Supplementary Note 6: Realization of duality and self-duality groups with 3D acoustic metamaterials

To explore the $\mathbb{Z}_2$ gauge model in a 3D acoustic metamaterial platform, we construct a tight-binding model with a 3D cubic lattice configuration. As a representative example, the self-dual lattice shown in Fig. S7(a) carries a total gauge flux of 6π, comprising eight sites (depicted as gray spheres) and twelve nearest-neighbor coupling bonds. This lattice is physically realized by the acoustic metamaterial illustrated in Fig. S7(b). The lattice constants are denoted as a_0 in the x and y directions, and h in the z direction. Each cuboid cavity has a length l_0, width w_0, and height h_0. The red cuboid coupling

tubes are characterized by a side length d_0, and the blue cylindrical coupling tubes by a radius r_0. The structural parameters are $a_0 = 56$ mm, $h = 40$ mm, $l_0 = 25$ mm, $w_0 = 15$ mm, $h_0 = 12$ mm, $d_0 = 3$ mm, and $r_0 = 2$ mm. This design strategy enables the physical realization of tight-binding models with precisely tailored couplings and gauge flux using acoustic metamaterials.

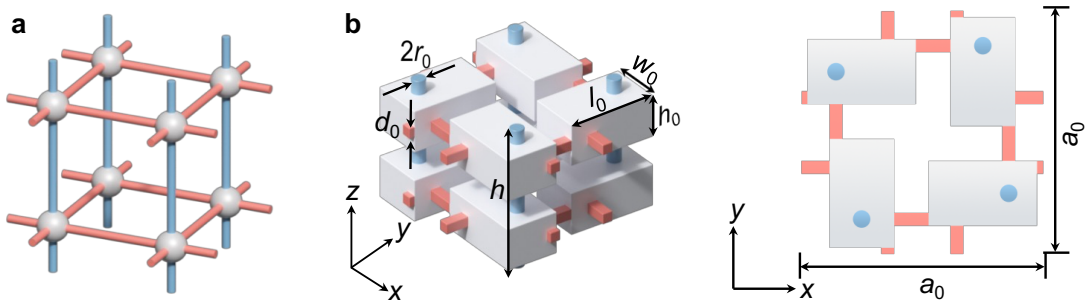

Fig. S7. Realization of a duality lattice in a 3D acoustic metamaterial. (a) Tight-binding configuration of a self-dual lattice carrying 6π gauge flux. (b) Perspective view (left) and top view (right) of the corresponding metamaterial unit cell. The lattice constants are $a_0 = 56$ mm (along x and y directions) and h =40 mm (along z direction). Each gray cuboid cavity, with width w_0, length l_0, and height h_0, acts as a lattice site (gray sphere) in the tight-binding model. Positive and negative couplings are realized by red cuboid coupling tubes (side length d_0) and blue cylindrical tubes (radius r_0), respectively.

The tight-binding configurations for lattices carrying 0, 2π, 4π, and 6π gauge flux are shown in Figs. S8(a)-(d), respectively. Their corresponding acoustic metamaterial implementations are illustrated in Figs. S8(e)-(h). Notably, positive coupling along the z-direction is achieved using tilted coupling tubes, which pose significant challenges for fabrication and experimental characterization. Therefore, it becomes necessary to investigate their physical properties through their dual counterparts. To solve the band structures of the 3D system, Floquet periodic boundary conditions are imposed on periodic surfaces of the unit cell along the x, y, and z directions; all other surfaces are applied by sound hard boundary conditions. The numerically simulated band structures of the acoustic metamaterials (green dots) are compared with the analytical band structures calculated from the tight-binding models (solid lines) in Figs. S8(i)-(l). As can be seen, the band structures of the configurations with 2π and 4π gauge flux exhibit

double degeneracy, while the configuration with 6π gauge flux exhibits fourfold degeneracy. In all cases, the simulated results show excellent agreement with the tight-binding model predictions.

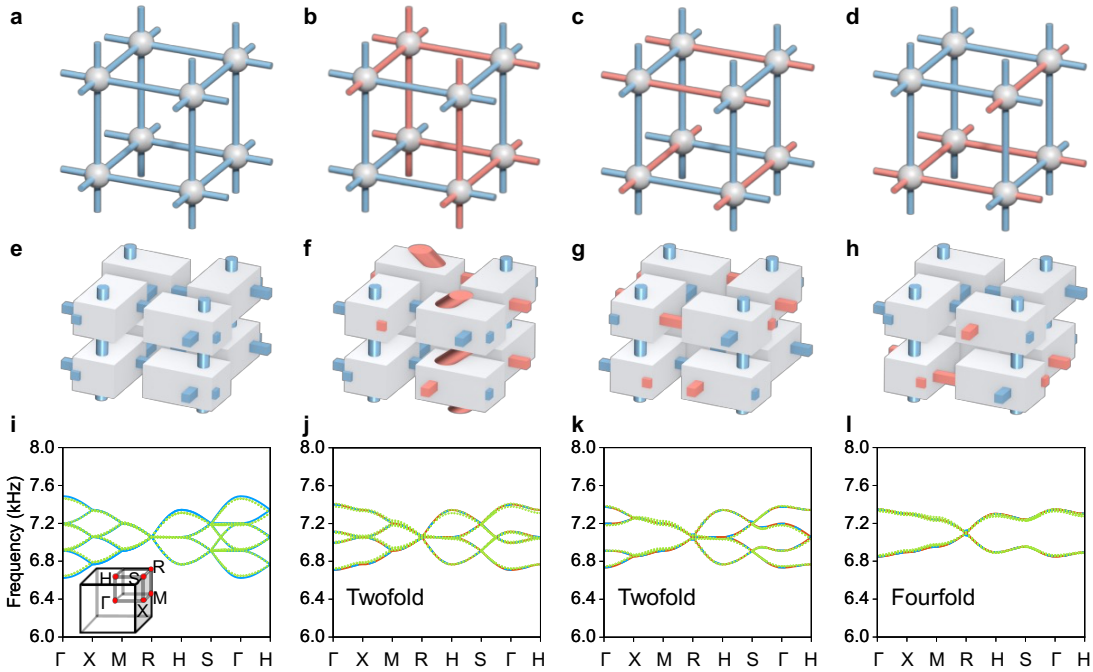

Fig. S8. Comparisons between the tight-binding models and acoustic metamaterials. (a)-(d): Tight-binding configurations for lattices with 0 gauge flux (a), 2π gauge flux (b), 4π gauge flux (c), and 6π gauge flux (d). (e)-(h): Corresponding realization in acoustic metamaterials of the tight-binding configurations in the top panel. (i)-(l): Comparison between band structures extracted from the tight-binding models (lines) and numerical simulations of the acoustic metamaterials (green dots).

Supplementary Note 7: Double Dirac point from the tight-binding model

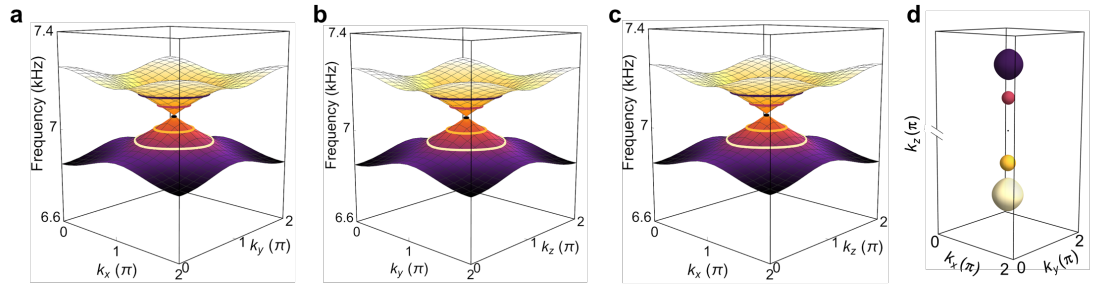

Fig. S9. (a)-(c) Calculated 3D band structures of the self-dual lattice with 6π gauge flux, plotted as functions of k_x, k_y, and k_z at fixed values of $k_z = \pi$ (a), $k_x = \pi$ (b), and $k_y = \pi$ (c), respectively. A clear double Dirac cone is observed at the band-crossing point near 7.08 kHz. (d) Iso-frequency contour surfaces at $f = 6.98$, 7.03, 7.08, 7.13, and 7.18 kHz, corresponding to the circular cross-sections indicated in (a)-(c). The

isotropic symmetry in $\boldsymbol{k}$-space illustrates the formation of a Dirac-like dispersion in all three orthogonal momentum planes.

Supplementary Note 8: Videos about the evolution of band structures as the coupling strength varies

Supplemental Video 1 illustrates the configurations and band structures of the two 2D acoustic metamaterials presented in Fig. 2 in the main text. The video showcases the evolution of band structures as the coupling strength varies. Specifically, as the coupling amplitudes along the x-direction evolve from both being positive (or both negative) to a configuration with one positive and one negative coupling, the system translates from a dual configuration to a self-dual configuration. Correspondingly, the band structure evolves from non-degenerate to double-degenerate bands.

Supplementary Note 9: Construction of the duality group

In our definition, two configurations ($|\Phi_m\rangle$) and ($|\Phi_k\rangle$) with equal flux are considered equivalent if they can be related by a global sign flipping $\mathcal{G}_i$, a space group symmetry G_p, or a combination of both. Specifically, this means that if one configuration can be transformed into the other by flipping the signs (colors) of all bonds, by performing a point group operation, or by combining these two operators, then they are equivalent i.e., $g|\Phi_m\rangle = |\Phi_k\rangle$, $g \in G_p \otimes \mathcal{G}$. Otherwise, the two configurations are inequivalent. Since the gauge-transformation operator U acts on these configurations, once an initial configuration is chosen, all other configurations with the same flux can be generated by the action of U. This definition naturally incorporates both the point-group symmetry G_p and the global sign flipping $\mathcal{G}$ into U, as U, G_p, and $\mathcal{G}$ mutually commute with each other. In other words, the group multiplication rule for these elements is $U_i \circ U_j = gU_k$.

In the 1D case, where only the change of hopping signs in the x-direction is considered, the dual operator U generates a $\mathbb{Z}_2$ group. In the 2D case, when hopping sign changes are allowed along both the x- and y-directions, application of Burnside's lemma combined with gauge-equivalence considerations yields three distinct classes

for flux-0 configurations and a single class for flux-π. For flux-0, three nontrivial dual operators [U_1 = diag$(1,-1,1,-1)$, U_2 = diag$(1,1,-1,1)$, U_3 = diag$(1,-1,-1,-1)$] relate the inequivalent configurations together with the identity $U_0 = diag(1,1,1,1)$, forming the $\mathbb{Z}_2 \otimes \mathbb{Z}_2$ duality group. The multiplication table is shown below.

	U_0	U_1	U_2	U_3
U_0	U_0	U_1	U_2	U_3
U_1	U_1	U_0	U_3	U_2
U_2	U_2	U_3	U_0	U_1
U_3	U_3	U_2	U_1	U_0

Table. 1 Multiplication table of gauge transformation U_i

In the 3D case, where there are 2^{12} configurations, under the equivalence rules we defined, 32 inequivalent configurations are obtained. After defining the bulk flux (the sum of the fluxes on the six faces), we obtain four classes: 0, 2π, 4π, and 6π. Further, for the flux 0 configurations, the dual configurations can be related by sixty-four U's (plus the identity $U = diag(1,1,1,1,1,1,1,1)$), This group has six generators, which are $U_1 = diag(1,1,-1,1,-1,1,1,1)$, $U_2 = diag(1,-1,1,1,1,1,1,-1)$, $U_3 = diag(1,1,1,-1,1,-1,1,1)$, $U_4 = diag(-1,1,-1,1,-1,1,1,-1)$, $U_5 = diag(-1,-1,1,1,1,-1,1,-1)$, $U_6 = diag(-1,1,-1,1,-1,-1,1,-1)$. Forming the group $G_U = \bigotimes_6 \mathbb{Z}_2 = \mathbb{Z}_2 \otimes \mathbb{Z}_2 \otimes \mathbb{Z}_2 \otimes \mathbb{Z}_2 \otimes \mathbb{Z}_2 \otimes \mathbb{Z}_2$.

References

[1] Zhao, Y. X., Huang, Y.-X. & Yang, S. A. Z_2-projective translational symmetry protected topological phases. *Phys. Rev. B* **102**, 161117 (2020).

[2] Zhao, Y. X., Chen, C., Sheng, X.-L. & Yang, S. A. Switching spinless and spinful topological phases with projective PT symmetry. *Phys. Rev. Lett.* **126**, 196402 (2021).

[3] Chen Z. Y., Yang, S. A. & Zhao Y. X. Brillouin Klein bottle from artificial gauge fields. *Nat. Commun.* **13**, 2215 (2022).

[4] Li, T. *et al*. Acoustic Möbius insulators from projective symmetry. *Phys. Rev. Lett.* **128**, 116803 (2022).

[5] Xue, H. *et al*. Projectively enriched symmetry and topology in acoustic crystals. *Phys. Rev. Lett.* **128**, 116802 (2022).

[6] Chen, Z. Y., Zhang, Z., Yang, S. A. & Zhao, Y. X. Classification of time-reversal-invariant crystals with gauge structures. *Nat. Commun.* **14**, 743 (2023).

[7] Y. Meng, *et al*. Spinful topological phases in acoustic crystals with projective *PT* symmetry. *Phys. Rev. Lett.* **130**, 026101 (2023).
[8] Zhu, Z. *et al*. Brillouin Klein space and half-turn space in three-dimensional acoustic crystals. *Sci. Bull.* **69**, 2050-2058 (2024).
[9] Qi, Y. *et al.* Acoustic realization of quadrupole topological insulators. *Phys. Rev. Lett.* **124**, 206601 (2020).